

1 **Removing ENSO’s influence from global SST variability, with** 2 **insights into the record-setting marine heatwaves of 2023-2024**

3
4 **Jacob L. Gunnarson¹, Yuxin Wang^{2,3,4}, Alessandro Gagliardi⁵, Darren L.C.Y. Li Shing**
5 **Hiung^{3,4}, Naoya Takahashi^{6,7}, Joel Wong⁸, Dillon J. Amaya⁹, Clara Deser¹⁰**

6
7 ¹ Department of Oceanography, University of Hawai‘i at Mānoa, Honolulu, Hawai‘i

8 ² Cooperative Institute for Marine and Atmospheric Research, University of Hawai‘i at Mānoa,
9 Honolulu, Hawai‘i

10 ³ Institute for Marine and Antarctic Studies, University of Tasmania, Hobart, Australia

11 ⁴ Australian Research Council Centre of Excellence for Climate Extremes, University of
12 Tasmania, Hobart, Australia

13 ⁵ Paleoclimate Dynamics Group, Alfred Wegener Institute, Helmholtz Centre for Polar and
14 Marine Research, Bremerhaven, Germany

15 ⁶ Department of Science, Niigata University, Niigata, Japan

16 ⁷ International Pacific Research Center, University of Hawai‘i at Mānoa, Honolulu, Hawai‘i

17 ⁸ Environmental Physics, Institute of Biogeochemistry and Pollutant Dynamics, ETH Zurich,
18 Zürich, Switzerland

19 ⁹ Physical Sciences Laboratory, Earth System Research Laboratory, National Oceanic and
20 Atmospheric Administration, Boulder, Colorado

21 ¹⁰ National Center for Atmospheric Research, Boulder, Colorado

22 23 **Capsule**

24 The 2023-2024 El Niño was partially responsible for the widespread marine heatwaves of 2023
25 and 2024.

26 27 **Abstract**

28 The El Niño-Southern Oscillation (ENSO) is a dominant driver of seasonal-interannual climate
29 variability and has been linked to record-setting extremes such as marine heatwaves (MHWs).
30 However, quantifying the effects of ENSO on MHW characteristics remains a challenge due to
31 data limitations. Here, we use an ensemble of tropical Pacific “Pacemaker” simulations with a
32 fully-coupled Earth System Model as a testbed for assessing the skill of four empirical methods
33 aimed at isolating ENSO’s contribution to monthly SST anomalies including MHW extremes. We
34 then apply the most skillful method to the observational record to determine ENSO’s impact on
35 the spatial coverage, intensity and duration of MHWs since 1960 (after removing the background
36 warming trend). We find that the El Niño of 2023-2024 contributed to about half of the global
37 coverage of record-setting MHWs, with the tropical Indian and tropical Atlantic Oceans being

38 most clearly impacted. Our results shed light on the critical role ENSO plays in driving the most
39 severe MHW conditions in the historical record.

40

41 **1. Introduction**

42 Through its far-reaching teleconnections, the El Niño-Southern Oscillation (ENSO) phenomenon
43 influences sea surface temperature (SST) variability well beyond the equatorial Pacific, making it
44 among the most important drivers of warm water extremes or marine heatwaves (MHWs) (Oliver
45 et al., 2018). MHWs can have severe ecological and socioeconomic impacts, hence the study of
46 their drivers is of critical importance for climate resilience and adaptation. ENSO’s relationship
47 with MHWs was put into sharp focus in 2023 and early 2024, as record-breaking ocean
48 temperatures were observed around the globe in conjunction with a strong El Niño event (Huang
49 et al., 2024; Jiang et al., 2024, 2025; Johnson et al., 2024), leading many to draw a causal link
50 between the phenomena.

51 One way to quantify this possible link is to statistically remove the ENSO signal from the
52 2023-2024 SST anomalies (SSTAs), and then recompute MHW characteristics. Many approaches
53 for removing the ENSO signal from climate data have been proposed over the years, for example
54 through linear regression on an ENSO index (Chiang & Vimont, 2004; Robock & Mao, 1995;
55 Santer et al., 2001) or empirical eigenmodes related to ENSO (Compo & Sardeshmukh, 2010;
56 Huang et al., 2024; Kelly & Jones, 1996), constructing a stochastic climate model for SST
57 tendencies that explicitly resolves ENSO forcing (Gunnarson et al., 2024), and using a Linear
58 Inverse Model (LIM) to filter out ENSO’s dynamical evolution (Solomon & Newman 2011).
59 However, there has yet to be a systematic comparison of the efficacy of these methods.

60 In this study we used an ensemble of Community Earth System Model version 2 (CESM2)
61 Tropical Pacific Pacemaker simulations to judge how well each of the four methods above removes
62 the “true” ENSO signal from the simulated SSTAs. We then applied the most skillful of these
63 methods to the observational record to estimate the influence of ENSO on record-breaking MHWs
64 since 1960, with a particular emphasis on the strong El Niño event of 2023-2024. As this work
65 focuses on internal climate variability and its relationship to ENSO, we looked at MHWs defined
66 after removing the anthropogenic warming trend.

67

68 **2. Data and Methods**

69 *(a) Tropical Pacific Pacemaker simulations and observational datasets*

70 To evaluate the efficacy of different ENSO-removal methods, we used the CESM2 Tropical
71 Pacific Pacemaker (CESM2-TPACE) experiments. CESM2-TPACE is based on CESM2
72 (Danabasoglu et al., 2020), and consists of 10 ensemble members from 1880 to 2019 at $\sim 1^\circ$
73 horizontal resolution, each with slightly different initial conditions and forced with historical
74 radiative forcing from 1880-2014 and SSP3-7.0 from 2015-2019. In addition, each member’s
75 equatorial Pacific SSTAs were nudged to observations using the Extended Reconstructed Sea
76 Surface Temperature Version 5 dataset (ERSSTv5; Huang et al., 2017), while the rest of the globe
77 evolved freely (the outline of the nudging region is shown in Appendix Figs. A1 and A2). As a
78 result, outside of the nudging region, SSTA variability in the CESM2-TPACE ensemble mean $\langle T' \rangle$
79 can be considered the “true” influence of observed tropical Pacific SSTA variability on global
80 climate (as simulated by the model), plus the influence of the external radiative forcing common
81 to each member (see also Deser et al., 2017). To isolate the contribution from ENSO, we further
82 remove the radiatively-forced component by subtracting the ensemble mean of the CESM2 Large
83 Ensemble (CESM2-LE; Rodgers et al., 2021) at each location and time, using the 50 members that
84 were driven by the same radiative forcing as used in CESM2-TPACE (i.e., the members that used
85 the CMIP6 biomass burning protocol).

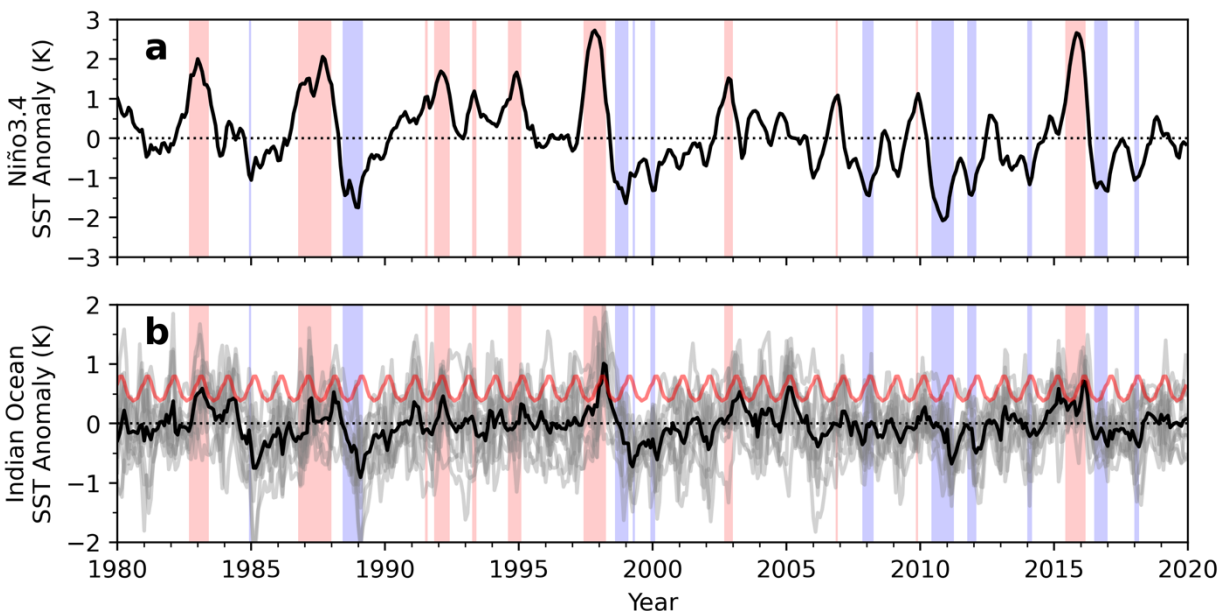
86 Timeseries of “ENSO-free” SSTAs in each member of CESM2-TPACE at each location
87 and time can then be calculated as:

$$88 \quad T'_{EF} = T' - \langle T' \rangle, \quad 1$$

89 where T' is the total SSTA and T'_{EF} represents simulated the “ENSO-free” SSTA that is
90 independent of both ENSO’s influence and external radiative forcing following the procedures
91 outlined above. The variable T'_{EF} , in particular, is a useful baseline by which to compare each
92 ENSO-removal technique. Specifically, we apply each ENSO-removal method to T' , generating
93 several estimates of T'_{EF} that can be used to quantitatively assess the efficacy of each method.
94 However, $\langle T' \rangle$ contains a non-zero residual from non-ENSO internal variability due to the small
95 ensemble size (Rowell et al., 1995), which we corrected for (see the Appendix for more
96 information). Fig. 1 shows an example of T' and $\langle T' \rangle$ for a single location in CESM2-TPACE.

97 We emphasize that the pacemaker experiment was used only to test the different methods.
98 CESM2 exhibits realistic ENSO teleconnections, even with its own internally-generated (and
99 somewhat biased) ENSO dynamics (Capotondi et al., 2020), hence we consider CESM2-TPACE

100 to offer a realistic testbed for our methods. For the results presented in Section 3, the methods were
 101 applied to observational data, and thus do not carry over any model biases present in CESM2-
 102 TPACE.
 103



104
 105 **Fig. 1** ENSO and Indian Ocean SSTA time series in the CESM2 Tropical Pacific Pacemaker
 106 experiment. (a) The ensemble-mean Niño3.4 SST index (black curve; note that all ensemble
 107 members have nearly identical ENSO indices by design). Red and blue shading indicate El Niño
 108 and La Niña events, respectively (events are defined based on when the Niño3.4 index exceeds
 109 one or is less than minus one standard deviation, respectively). (b) SSTA timeseries at 30°S, 80°E
 110 in the Indian Ocean, selected as an illustrative example of a location that is highly correlated with
 111 the Niño3.4 index. Individual ensemble members (T') are shown in grey, and the ensemble mean
 112 ($\langle T' \rangle$) in black. The red curve indicates the seasonal 90th-percentile threshold used to calculate
 113 marine heatwaves.

114
 115 In our evaluation of observed MHW conditions, we use the Hadley Center Global Sea Ice
 116 and Sea Surface Temperature v1.1 dataset of monthly-mean SST at 1° spatial resolution (HadISST;
 117 Rayner et al., 2003) from January 1960 to November 2024. Monthly anomalies were calculated
 118 by removing the climatology for each month separately and then removing the background trend
 119 by subtracting the least damped eigenmode using a Linear Inverse Model (LIM) analysis (see Xu
 120 et al., 2022). We did not analyze grid points which had missing SST data (e.g., from sea ice
 121 coverage). We also used sea level pressure data from the ECMWF Reanalysis v5 (ERA5; Hersbach
 122 et al., 2020), with anomalies calculated by subtracting the monthly climatology and a linear trend.

123

124 *(b) Methods for removing the influence of ENSO*

125 A brief summary of each of the four methods is provided below; details may be found in the
126 Appendix.

127

128 *(i) Linear Regression on the Niño3.4 SST index*

129 The simplest (and most widely used) method for removing ENSO is to assume that SSTAs consist
130 of a component driven by internal variability independent of ENSO and a component which is a
131 linear function of the ENSO state, in this case given by the Niño3.4 SST index (the average SSTAs
132 over 5°N-5°S, 170°W-120°W; Barnston et al., 1997). The ENSO component of SSTAs is found
133 via linear regression onto the Niño3.4 SST index. Because of the large thermal inertia of the ocean
134 mixed layer, the peak correlation between SSTAs and Niño3.4 usually occurs when Niño3.4 leads
135 by a few months (e.g., Alexander et al., 2002). Thus, we evaluated the regression method at two
136 different leads: 0 and 3 months.

137

138 *(ii) EOF Removal*

139 The second method is a more general version of the first method, employing Principal
140 Component (PC) timeseries associated with the leading Empirical Orthogonal Function (EOF)
141 spatial patterns of global SSTAs in place of the single Niño3.4 SST index (Huang et al., 2024;
142 Kelly & Jones, 1996). We evaluated the optimal number of EOFs/PCs to remove based on the
143 metrics outlined in Section 2c.

144

145 *(iii) Tendency Regression*

146 The third method uses an extension of the original stochastic climate model developed by
147 Hasselmann, (1976):

148

$$149 \quad \frac{dT'(t)}{dt} = \lambda T'(t) + \beta N(t) + \xi(t), \quad 2$$

150

151 where λ is a feedback (damping) coefficient, β is an ENSO teleconnection coefficient, $N(t)$ is an
152 ENSO index (in this case Niño3.4), and $\xi(t)$ is stochastic (white noise) forcing. Similar models

153 have been successfully used to assess the remote influence of ENSO on modes of SST variability
 154 such as the Pacific Decadal Oscillation (Newman et al., 2003, 2016; Schneider & Cornuelle,
 155 2005) and Indian Ocean Dipole (Stuecker et al., 2017; S. Zhao et al., 2019) as well as on North
 156 Pacific SST variability in general (Gunnarson et al., 2024; Park et al., 2006). Both λ and β have
 157 seasonally-modulated values, allowing Eq. 2 to represent dynamics such as the ENSO
 158 combination modes (Stuecker et al., 2013). To construct SST anomalies without the influence of
 159 ENSO, Eq. 2 is fit to the data at each grid point via multiple linear regression and then integrated
 160 forward in time without the ENSO teleconnection term.

161
 162 *(iv) LIM Filter*
 163 The fourth method uses a Linear Inverse Model (LIM) to construct an optimal perturbation filter
 164 following Solomon & Newman (2012). The LIM assumes the SST dynamics can be represented
 165 as a linear system forced by stochastic forcing (Penland & Sardeshmukh, 1995),

$$\frac{dx}{dt} = Lx + \xi, \quad 3$$

166
 167
 168
 169 where x is the state vector of the system (i.e., SSTAs at different times and locations in this study),
 170 L is the dynamical operator matrix describing the dynamical features of the evolution of x , and ξ
 171 is the stochastic forcing vector. For a given initial state $x(t)$, the most likely state \hat{x} at time $t+\tau$ is

$$\hat{x}(t + \tau) = \exp(L\tau) x(t). \quad 4$$

172
 173
 174
 175 The LIM methodology objectively determines the “optimal initial condition” that evolves into a
 176 final specified condition (e.g., mature ENSO). L is generally non-normal, with orthogonal
 177 eigenvectors (Penland & Matrosova, 2006), allowing transient anomaly amplification through
 178 constructive eigenmode interference before anomalies eventually decay. The “optimal initial
 179 condition” is the condition that maximize the state vector amplification (Penland & Sardeshmukh,
 180 1995). Following Solomon & Newman (2012), we use LIM to remove the ENSO signal from
 181 SSTAs by filtering out the variability that evolves from the optimal initial condition of a mature
 182 ENSO event through the next mature ENSO event.

183

184 *(c) Evaluation Metrics*

185 We used two metrics to assess how well each method performed at removing the influence of
186 ENSO from the SSTA field: 1) the lagged correlation with Niño3.4 index with the ENSO-removed
187 SSTAs; and 2) comparison of the variance of the ENSO-removed SSTA field with that of the
188 “ENSO-free” SSTAs from the pacemaker experiment (see Eq. 1). A perfect method would show
189 zero correlation with Niño3.4 at all lags and would have the same variance as the ENSO-free
190 SSTAs.

191
192 *(d) MHW definitions*

193 MHWs can be defined in several ways, particularly in regard to fixed versus shifting baselines
194 (Amaya et al., 2023; Smith et al., 2025). As our study is concerned with ENSO’s influence on
195 internal climate variability and not the mean state change, we use a shifting baseline (i.e., by
196 subtracting the pattern of mean state change; see Section 2a). In this study, we define a MHW as
197 any month which exceeds the 90th-percentile of SSTAs for that calendar month in a given grid cell.
198 We compute the MHW thresholds using the full SSTAs (i.e., before removing the influence of
199 ENSO).

200 MHW duration is defined as the number of consecutive months in a grid cell that
201 experience MHW conditions (note that this definition is different than for daily data). Because of
202 the limited observational time span, we smooth the data spatially by computing the mean and
203 extremes (97.5th-percentile) of the MHW durations in 5°x5° bins. MHW intensity is calculated by
204 summing the SSTAs of MHWs in a grid cell and then dividing by the total number of months in
205 the dataset (expressed in units of °C-weeks/year, analogous to degree heating weeks). As this is an
206 integrated value which is less noisy than the duration statistics, spatial binning is unnecessary.

207

208 **3. Results**

209 *(a) ENSO’s fingerprint*

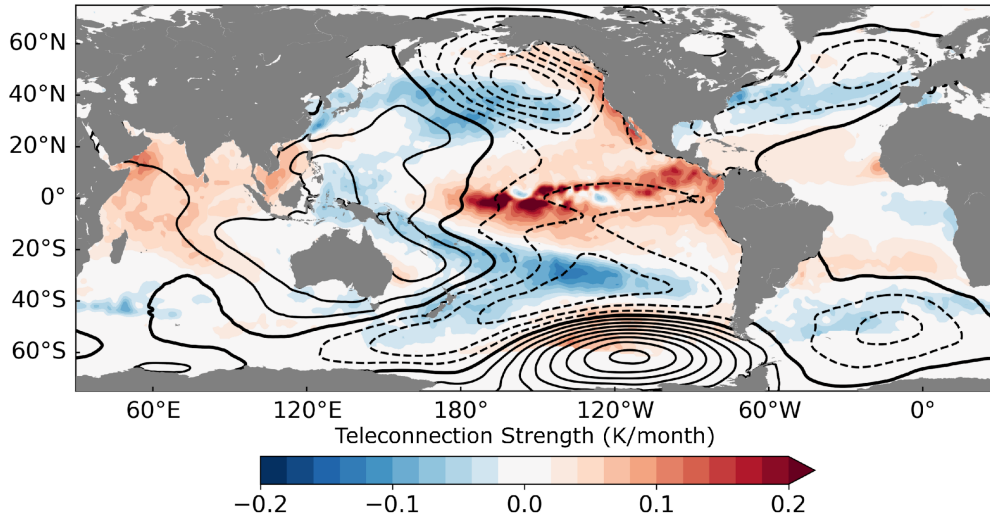
210 Of the four methods to remove ENSO’s influence on SSTAs outlined in Section 2b, the SST
211 Tendency Regression and LIM Filter performed the best and showed comparable skill (see the
212 discussion in the Appendix). Because the Tendency Regression method is much simpler to
213 implement and was slightly better at removing the influence of ENSO compared to the LIM Filter
214 method, we present results based on that approach in the main text; however, very similar results

215 were found using LIM Filter (Supplementary Figs. S1-S3). The Linear Regression method (with a
216 3-month lead) removed the Niño3.4 correlation reasonably well but had variance well in excess of
217 the “true” ENSO-free variance. The EOF Removal method (with two or three EOFs removed)
218 reproduced the ENSO-free variance the best out of all of the methods, but was worse at removing
219 the Niño3.4 correlation than the Tendency Regression or LIM Filter methods.

220 Based on these results, we applied the Tendency Regression method to observed SSTAs to
221 quantify the impact of ENSO on MHWs over the historical record (since 1960) as well as the
222 influence of the most recent El Niño on the record-breaking MHWs observed in 2023 and early
223 2024.

224 Although the Tendency Regression method is an empirical statistical approach for
225 quantifying ENSO’s remote influence on SSTA, its results are in good correspondence with
226 previous literature on the dynamics of ENSO teleconnections. In particular, the spatial pattern of
227 ENSO-induced SSTA forcing obtained with the Tendency Method (Fig. 2) is similar to that found
228 in previous studies (e.g., Alexander et al., 2002; Lau & Nath, 1994, 1996) with (during El Niño) a
229 “horseshoe” pattern of cooling in the North and South Pacific, warming in the Indian Ocean, and
230 warming in the subtropical North and South Atlantic with cooling poleward. Atmospheric
231 circulation anomalies correlated with ENSO overlie these warming and cooling patterns: the so-
232 called “atmospheric bridge” linking extratropical SSTs with the equatorial Pacific via atmospheric
233 Rossby waves. For example, in the North Pacific a dipole pattern with cooling in the center of the
234 basin and warming along the west coast of North America is associated with a deepening of the
235 Aleutian Low. As established by previous studies, the cold and dry air advected along the western
236 side of this atmospheric circulation anomaly cools the ocean during El Niño, with warm and humid
237 air advected along the eastern side of the circulation anomaly, leading to ocean warming
238 (Alexander et al., 2002). Similar teleconnection patterns are present in the South Pacific and North
239 and South Atlantic. In the equatorial Indian and Atlantic oceans, modulations of the Walker
240 circulation link SSTAs to ENSO (see Taschetto et al., 2020 for a review of ENSO atmospheric
241 teleconnections).

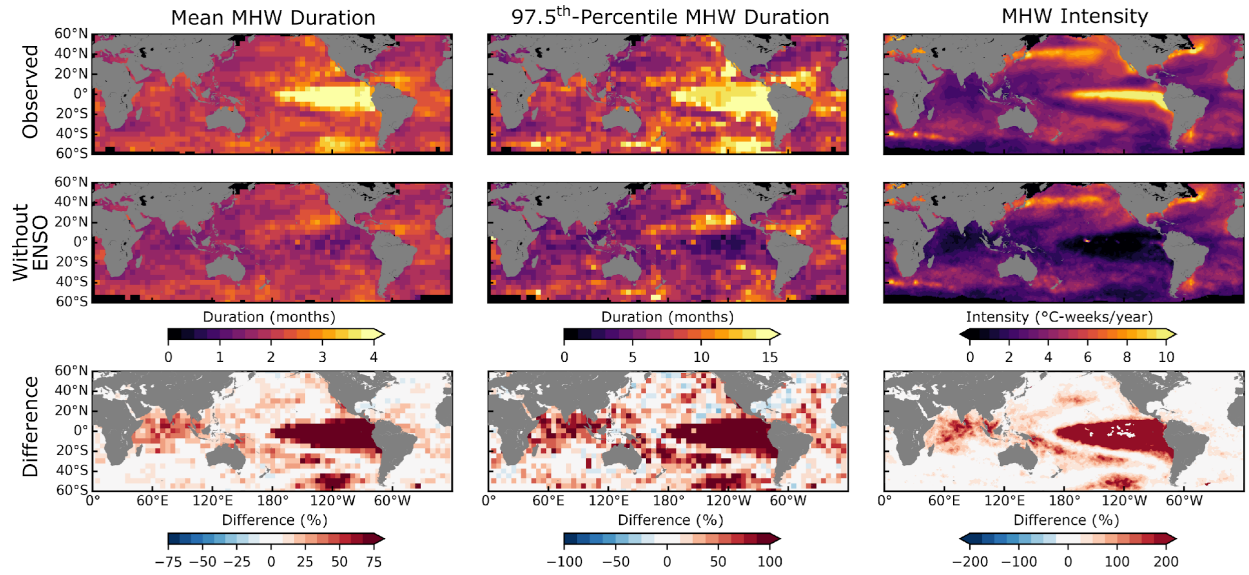
242



243
 244 **Fig. 2.** ENSO teleconnection strength in the HadISST observational dataset using the Tendency
 245 Regression method. The teleconnection strength (color shading; K/month) is the annual average
 246 of the teleconnection coefficient β multiplied by the standard deviation of the Niño3.4 Index, which
 247 represents a typical value for the remote forcing during an El Niño event. As discussed in the
 248 Appendix, the Tendency Regression method cannot reproduce ENSO itself, thus the
 249 teleconnection strength in the equatorial Pacific is not physically meaningful. The contours show
 250 the regression of ERA5 sea level pressure on the Niño3.4 index, with dashed contours representing
 251 negative values, a contour interval of 30 Pa/K, and a thicker line at 0 Pa/K.
 252

253 *(b) Impact of ENSO on observed MHW duration and intensity*

254 The influence of ENSO on observed MHW duration (mean and extreme) and intensity during
 255 1960-2024 is shown in Fig. 3. ENSO acts to increase MHW duration and intensity almost
 256 everywhere, in agreement with previous work (Oliver et al., 2018). The largest increases in both
 257 duration and intensity due to ENSO, excepting the equatorial Pacific itself, occur in regions
 258 strongly influenced by ENSO teleconnections, in particular the tropical Indian and Atlantic sectors,
 259 and a horseshoe-like pattern in the North and South Pacific. On average over the global oceans
 260 between 60°S and 60°N (excluding the equatorial Pacific: 20°S-15°N, 160°E-70°W), ENSO
 261 increases the mean MHW duration by 9.2% and increases the extreme (97.5th-percentile) MHW
 262 duration by 23.9%. In areas of strong ENSO influence, the increase in mean MHW duration can
 263 be over 50% and the 97.5th-percentile duration can increase by over 100%. The latter is reflective
 264 of ENSO's influence on very persistent, but rare, MHWs (see Supplementary Fig. S4). The global
 265 average MHW intensity is 2.27 °C-weeks/year without ENSO and 2.78 °C-weeks/year with
 266 ENSO, an increase of 22.5%, although in areas of high teleconnection strength in the Pacific and
 267 Indian oceans, the increase in intensity can exceed 100%.



269

270 **Fig. 3.** ENSO’s influence on the mean and extreme (97.5th percentile) durations of MHWs and the
 271 mean intensity of MHWs during 1960-2024 based on the HadISST data set. (Top row) Observed;
 272 (Middle row) After removing the influence of ENSO using the Tendency Regression method; and
 273 (Bottom row) Their difference (e.g., ENSO influence, shown as a percentage of the ENSO-
 274 removed value). Duration is calculated using 5°x5° bins. MHW intensity is the sum of the MHW
 275 SSTAs divided by the number of years in the data in a given grid cell (°C-weeks/year). Note the
 276 different color bar ranges in the difference panels.

277

278 (c) Impact of ENSO on observed MHW spatial coverage

279 The area of the global oceans covered by MHWs at any given time is also greatly affected by
 280 ENSO. By defining MHWs using a 90th-percentile threshold, we expect ~10% of the oceans to
 281 experience a MHW at any given time due to random chance. However, our results indicate that El
 282 Niño tends to greatly increase observed MHW spatial coverage beyond the equatorial Pacific (Fig.
 283 4). To quantify this effect, we define A_{obs} and A_{TR} as the areal percentage of the global ocean (60°S-
 284 60°N, excluding the equatorial Pacific) with MHW conditions before and after removing ENSO
 285 (using the Tendency Regression method), respectively. We also define a “signal-to-noise ratio” as

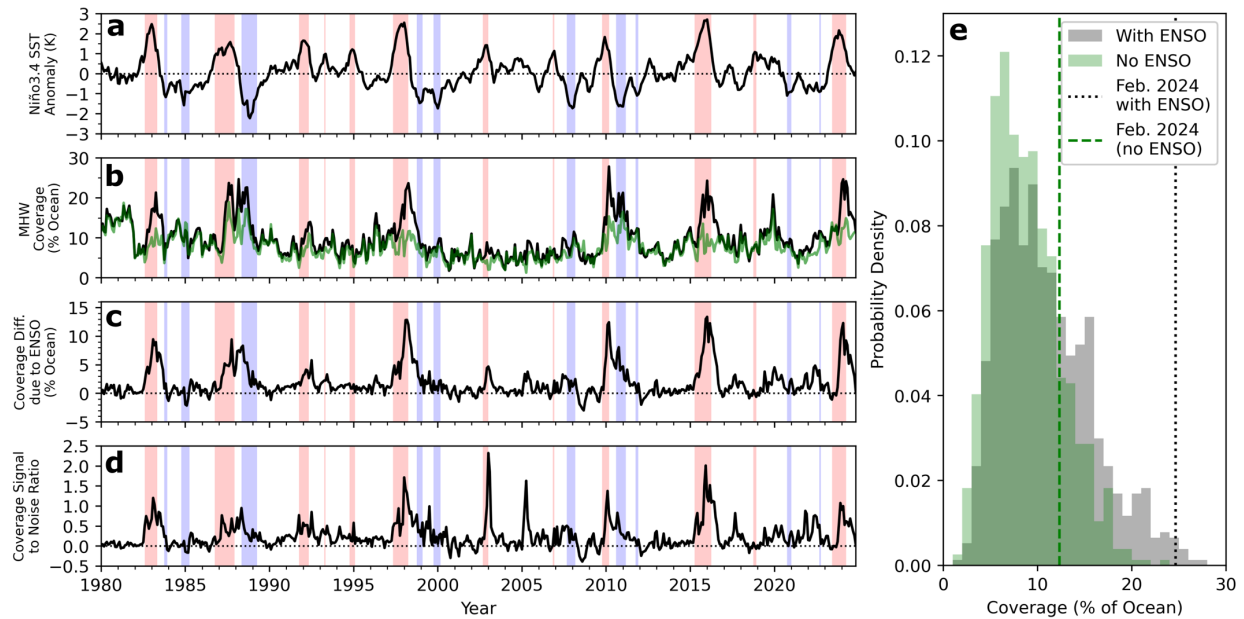
286

$$287 \quad SNR = \frac{A_{obs} - A_{TR}}{A_{TR}}. \quad 5$$

288

289 The SNR represents the contribution from ENSO to the global MHW area relative to the
 290 contribution from unrelated internal variability.

291



292

293 **Fig. 4.** ENSO's influence on the spatial coverage of MHWs based on the HadISST dataset. (a)
 294 Niño3.4 index. El Niño events are shaded red and La Niña events are shaded blue). (b) Areal
 295 percentage of the global ocean (60°S-60°N, excluding the equatorial Pacific: 20°S-15°N, 160°E-
 296 70°W) with MHW conditions before (A_{obs} ; black curve) and after removing ENSO using the
 297 Tendency Regression method (A_{TR} ; green curve). (c) $A_{obs} - A_{TR}$. (d) The ENSO “signal-to-noise”
 298 ratio (SNR). (e) Probability density function of A_{obs} (grey) and A_{TR} (green). The February 2024
 299 MHW A_{obs} and A_{TR} values are indicated by the dotted gray and dashed green lines, respectively.

300

301 During El Niño events, A_{obs} spikes, with peak values between 21% - 27% (24.6% in
 302 February 2024; Fig. 4b, black curve). These spikes are greatly reduced or non-existent for A_{TR} (Fig.
 303 4b, green curve), as confirmed by the difference $A_{obs} - A_{TR}$ (Fig. 4c). The maximum MHW area
 304 coverage typically lags the peak of an El Niño event by several months, likely due to the effect of
 305 the ocean integrating the atmospheric forcing from the ENSO teleconnection. La Niña events do
 306 not appear to significantly affect MHW coverage, possibly due to their lesser amplitude compared
 307 to El Niño events. In other words, only El Niño creates a large enough signal to clearly emerge
 308 from the background noise of the climate system for this particular measure of global MHWs (note
 309 that La Niña can induce MHWs on a regional scale; e.g., Feng et al. (2013)).

310 The SNR also peaks during El Niño, although it reveals that some spikes in global MHW
 311 coverage appear to be due to a confluence of the effects of ENSO and random internal variability
 312 (Fig.4d). For example, the 1987-1988 El Niño had maximum SNRs of 1.0, indicating that the
 313 MHW coverage due directly to the El Niño was comparable in magnitude to that caused by other

314 forms of internal variability. In contrast, the 2015-2016 El Niño had the highest observed SNR of
315 2.2, thus about 2/3rd of the total MHW area was caused directly by the El Niño.

316 The 2023-2024 El Niño had a maximum SNR of 1.1 (in December 2023), with an SNR of
317 1.0 at the peak of the MHW coverage in February 2024 and an average of 0.7 between January
318 and May 2024. This suggests that internal variability unrelated to ENSO was roughly as important
319 in generating the extensive global MHW coverage during that event as the El Niño was.
320 Nevertheless, a histogram of MHW spatial coverage (Fig. 4e) shows that the maximum spatial
321 coverage of MHWs in 2023-2024 was beyond that caused by internal variability alone. Thus, the
322 widespread nature of MHWs in February 2024 could not have occurred without El Niño's
323 influence.

324

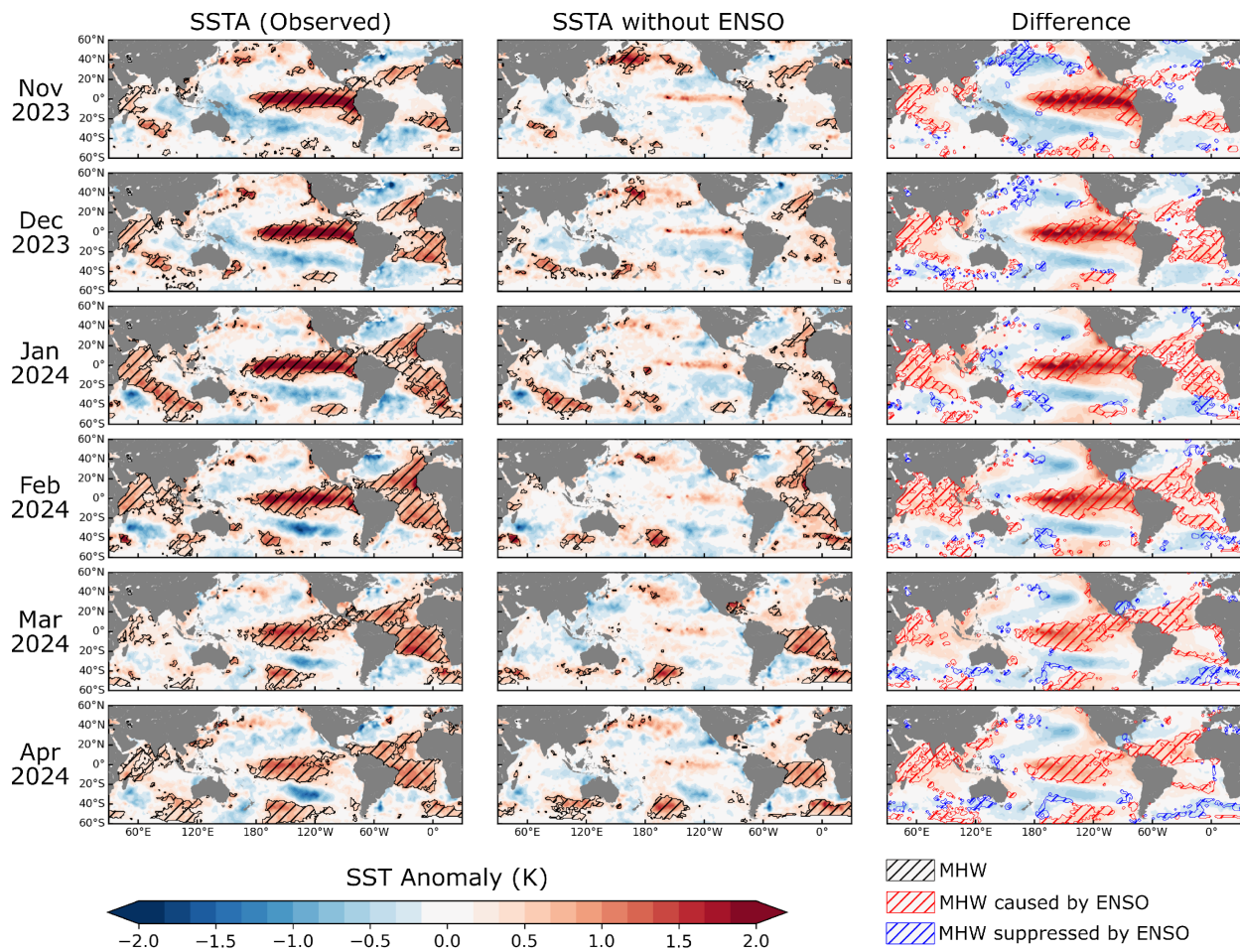
325 *(d) Impact of the 2023-2024 El Niño*

326 Fig. 5 shows the spatial structure and evolution of the 2023-2024 El Niño and its effect on global
327 MHWs (Supplementary Fig. S5 shows the same information for historical El Niño events). The
328 influence of ENSO (recall Fig. 2) can be gleaned by the difference between the observed SSTAs
329 and those computed via our Tendency Regression method. In the Indian Ocean, the El Niño
330 warmed the eastern half of the basin, leading to a positive-phase Indian Ocean Dipole (IOD) event
331 in the fall and winter of 2023, which then transitioned to basin-wide warming in early 2024. This
332 sequence and its relationship with ENSO is consistent with previous studies (Klein et al., 1999;
333 Saji et al., 1999; Stuecker et al., 2017). With ENSO's influence removed, the IOD pattern was
334 considerably diminished, and MHWs remained only in the southern Indian Ocean.

335

336

337



338

339 **Fig. 5.** Evolution of the 2023-2024 El Niño and associated MHWs. (Left column) observed SSTA
 340 from HadISST with MHWs outlined and hatched in black. (Middle column) SSTA and MHWs
 341 without the influence of ENSO calculated using the Tendency Regression method. (Right column)
 342 Difference between observed and ENSO-removed SSTA and MHW. Areas where ENSO's
 343 influence caused MHWs are outlined and hatched in red; areas where ENSO suppressed MHWs
 344 are outlined in hatched in blue.

345

346 The El Niño's role in the North Pacific was to suppress MHWs in the central part of the
 347 basin (in November and December 2023), and enhance them along the west coast of North
 348 America, a result of the positive phase of the Pacific Decadal Oscillation, which is strongly linked
 349 to ENSO (e.g., Newman et al., 2016; Schneider & Cornuelle, 2005). MHWs were enhanced in the
 350 South Pacific, likely a result of the Pacific-South American modes of atmospheric variability,
 351 which carry ENSO's influence to the South Pacific (Mo, 2000; Mo & Higgins, 1998).

352 In the Atlantic Ocean, a considerable portion of the MHW coverage during 2023-2024
 353 appears to have originated from internal variability unrelated to ENSO, as evidenced by the

354 sizeable MHW area that remains after ENSO's influence is removed, particularly in the South
355 Atlantic after February 2024 (Fig. 5, middle column). Nevertheless, the El Niño did lead to MHWs
356 in the tropical Atlantic as well as MHWs in the subtropical North and South Atlantic (Fig. 5, right
357 column). Warming in the tropical and subtropical North Atlantic has been linked to El Niño (e.g.,
358 Alexander & Scott, 2002; Huang, 2004) as has warming in the subtropical South Atlantic
359 (Rodrigues et al., 2011, 2015). Thus 2023-2024 MHWs in the Atlantic, which covered a large part
360 of the basin, originated from a confluence of ENSO and unrelated internal climate variability.

361

362 **4. Conclusions**

363 In this study we compared several empirical methods for removing the influence of ENSO from
364 global SSTAs using a “perfect model” approach, and then applied the most skillful method to
365 observed MHWs during 1960-2024 after removing the background warming trend. Using the
366 CESM2-TPACE experiments as a testbed, we concluded that the Tendency Regression and LIM
367 Filter methods are the most skillful at removing the influence of ENSO based on two metrics. The
368 Tendency Regression method is somewhat more flexible, simple to implement, and does not
369 require large-scale spatial data, which may be useful when additional climate modes or physical
370 processes are of interest or for situations when the data is sparse (e.g., paleoclimate studies).

371 Using the Tendency Regression method to remove the influence of ENSO from
372 observational SST data, we found that ENSO acts to increase the mean MHW duration by 9.2%
373 and the MHW intensity by 22.5%. The spatial coverage of MHWs spikes during El Niño events,
374 typically reaching an area of between 21% to 27% of the global ocean outside the equatorial Pacific
375 compared to 10% or less during non-El Niño years. By removing the influence of ENSO, we
376 confirmed that these spikes indeed are caused by El Niño events. About half of the MHW spatial
377 coverage in 2023-2024 was caused by the concurrent El Niño. Indeed, we find that the widespread
378 nature of MHWs in February 2024 could not have occurred without El Niño's influence.

379 The evolving spatial pattern of MHWs during the 2023-2024 El Niño follows closely
380 previously studied global ENSO teleconnections. During 2023-2024, MHWs in much of the Indian
381 Ocean were found to be attributable to the influence of El Niño, as was the suppression and
382 enhancement of MHWs in the North Pacific and enhancement of MHWs in the South Pacific. The
383 Atlantic MHWs, which covered a large part of the basin, were caused by a confluence of ENSO's
384 remote influence and unrelated internal variability.

385 Our results highlight the importance of ENSO in driving marine heatwaves worldwide.
386 However, there is little agreement across climate models on how ENSO has and will respond to
387 anthropogenic forcing (Maher et al., 2023). Thus, to understand how MHWs will change as the
388 world warms, accurate modeling of ENSO dynamics is crucial.

390 **Acknowledgements**

391 We would like to express our gratitude to the two anonymous reviewers for their constructive
392 comments. JLG acknowledges the support of the Uehiro Center for the Advancement of
393 Oceanography. The authors thank Drs. Michael Alexander, Malte Stuecker, and Tongtong Xu for
394 their helpful advice. We acknowledge the work of the CESM Climate Variability and Change
395 Working Group (CVCWG) and high-performance computing support from the Cheyenne system
396 () provided by the NSF National Center for Atmospheric Research (NCAR). We also acknowledge
397 the organizers and funders of the CLIVAR Marine Heatwave Summer School at the International
398 Centre for Theoretical Physics in Trieste, Italy, where the seeds of this paper were first planted.

400 **Data Availability Statement**

401 The Tropical Pacific Pacemaker and CESM2-LE data are available via the Earth System Grid
402 (<https://www.earthsystemgrid.org>), and the HadISST data are available from the Met Office
403 (<https://www.metoffice.gov.uk/hadobs/hadisst/>). The code and data to reproduce the figures in this
404 study are available via Zenodo (<https://doi.org/10.5281/zenodo.15015971>).

406 **Appendix**

407 Our methods for removing the influence of ENSO as well as our metrics for evaluating their
408 efficacy are outlined briefly in the main text (Section 2b-c). Here we present a detailed overview
409 and discussion of these methods.

411 *1. Linear Regression*

412 The simplest (and thus most widely used) method to remove the ENSO signal from SSTAs is to
413 assume that the anomaly can be separated into a component driven solely by internal variability
414 that is linearly independent of ENSO and a component which is a linear function of the ENSO
415 state:

416

$$417 \quad T'(t) = T'_{LR}(t) + rN(t - \tau), \quad A1$$

418

419 where T' is the total SSTA at a given location (as in Eq. 1), T'_{LR} is the SSTA resulting from internal
420 variability that is linearly independent of equatorial Pacific SST variability, r is a regression
421 coefficient, N is an ENSO index (e.g., Niño3.4) and τ is a time lag in months. We tested this method
422 for ENSO leads of $\tau=0$ months and $\tau=3$ months. To remove the ENSO signal, r is computed at
423 each grid point via linear regression and Eq. A1 is solved for T'_{LR} .

424

425 2. EOF Removal

426 Empirical Orthogonal Functions (EOFs) are widely used in climate science to identify leading
427 modes of variability. For example, the leading EOF of equatorial Pacific SSTAs is usually
428 identified as Eastern Pacific (EP) El Niño and the second EOF as Central Pacific (CP) El Niño
429 (e.g., Timmermann et al., 2018). By subtracting the leading EOFs from the SSTAs, the influence
430 of ENSO can be removed (Huang et al., 2024; Kelly & Jones, 1996).

431 In our analysis, we compute the first 50 global SSTA EOFs and corresponding Principal
432 Component (PC) time series. We then subtracted the first N EOFs from the original data:

433

$$434 \quad T'_{EOF}(x, y, t) = T'(x, y, t) - \frac{1}{w(y)} \sum_{n=1}^N EOF_n(x, y) PC_n(t), \quad A2$$

435

436 where T'_{EOF} is the ENSO-free SSTA, $w(y)$ is the area weighting used to compute the EOFs (the
437 cosine of the latitude y), EOF_n and PC_n are the n^{th} Empirical Orthogonal Function and Principal
438 Component, respectively. We tested a range of N when evaluating this method ($N=1$ to $N=4$).
439 Supplementary Fig. S6 shows the first four leading EOF spatial patterns for one member of the
440 Pacemaker ensemble.

441

442 3. Tendency Regression

443 The Tendency Regression method describes a model of ENSO's remote influence on SSTAs that
444 is constructed by adding an ENSO teleconnection term to the original local linear stochastic
445 climate model developed by Hasselmann, (1976):

446

447
$$\frac{dT'(t)}{dt} = \lambda T'(t) + \beta N(t) + \xi(t), \quad \text{A3}$$

448

449 where λ is a feedback (damping) coefficient, β is an ENSO teleconnection coefficient, and $\xi(t)$ is
 450 stochastic (white noise) forcing. Physically, the right-hand-side of Eq. A3 represents three
 451 processes: feedback (damping) by air-sea heat fluxes and oceanic processes (Frankignoul, 1985),
 452 forcing by the air-sea heat fluxes that result from ENSO-excited atmospheric planetary waves (i.e.,
 453 “atmospheric bridge”; Lau & Nath, 1996); and stochastic forcing by air-sea heat fluxes and
 454 anomalous Ekman advection of the mean SST gradient (Larson et al., 2018). Similar models have
 455 been successfully used to assess the remote influence of ENSO on modes of SST variability such
 456 as the Pacific Decadal Oscillation (Newman et al., 2003, 2016; Schneider & Cornuelle, 2005) and
 457 Indian Ocean Dipole (Stuecker et al., 2017; S. Zhao et al., 2019) as well as on North Pacific SST
 458 variability in general (Gunnarson et al., 2024; Park et al., 2006).

459 Taking into account seasonal modulations, the feedback and ENSO teleconnection
 460 coefficients are defined as

461

462
$$\lambda = \lambda_0 + \lambda_1 \sin(\omega_a t) + \lambda_2 \cos(\omega_a t), \quad \text{A4}$$

463
$$\beta = \beta_0 + \beta_1 \sin(\omega_a t) + \beta_2 \cos(\omega_a t), \quad \text{A5}$$

464

465 where ω_a is the angular frequency of the annual cycle ($2\pi/12$ months⁻¹) and λ_1 , λ_2 , β_1 , and β_2
 466 determine the amplitude and phase of the seasonal modulation of the teleconnection around the
 467 constants λ_0 and β_0 (De Elvira & Lemke, 1982; Nicholls, 1984; Stuecker et al., 2017).

468 To remove the ENSO signal, Eq. A3 is fitted to the SSTAs at each location using multiple
 469 linear regression. dT'/dt is then computed using forward finite differencing. The residual from the
 470 regression is ζ . Then a new SSTA time series is integrated without the ENSO teleconnection term:

471

472
$$T'_{TR}(k + 1) = T'_{TR} + [\lambda(m)T'_{TR}(k) + \xi(k)]\Delta t, \quad \text{A6}$$

473

474 where T'_{TR} is the SSTA forced only by stochastic noise, k is the time index, m is the month index
 475 (k modulo 12) and Δt is the time step (1 month). The integration is initialized with the SSTA at the
 476 start of the time period of the data (see Gunnarson et al. (2024) for further discussion). The spatial

477 pattern of the first EOF of ζ resembles ENSO and its teleconnections, albeit with a white-noise PC
478 time series, thus we remove the first EOF of ζ before integrating Eq. A6.

479 The advantage of the Tendency Regression method over the simple regression method is
480 that it more faithfully represents the physical processes that generate SSTAs. The persistence of
481 SSTAs forced by ENSO is directly modeled, eliminating the need for the lagged ENSO regression
482 in the simple regression method above. A limitation of this method is that it cannot remove remote
483 ENSO forcing that lags the ENSO time series, e.g. oceanic planetary waves excited by ENSO
484 (Sprintall et al., 2020). Additionally, it does not model the reemergence of SSTAs forced by ENSO
485 due to the seasonally-varying mixed layer depth in the extratropics (Alexander & Deser, 1995;
486 Newman et al., 2016). It also cannot replicate ENSO itself, but if one is interested in SSTAs outside
487 the equatorial Pacific, this is not a concern.

488

489 *4) Linear Inverse Model*

490 The LIM is used to describe the SSTAs system in the form of (Penland and Sardeshmukh,
491 1995):

492

$$493 \quad \frac{dx}{dt} = Lx + \xi, \quad A7$$

494

495 where x is the state vector of the system (i.e., SSTAs at different times and locations), L is the
496 dynamical operator matrix describing the dynamical features of the evolution of x , and ξ is the
497 stochastic forcing matrix. L can be calculated as

498

$$499 \quad L = \tau^{-1} \ln[C(\tau)C(0)^{-1}], \quad A8$$

500

501 where $C(0)$ and $C(\tau)$ are the covariance matrix of vector x at lag-0 and lag- τ , respectively.

502 The dimensionality of x is typically reduced via EOF analysis. We used the first 40 global
503 SSTA EOFs. The state vector $x(t)$ then consists of the first 40 PCs, which explains 70.2% of the
504 total global CESM2-TPACE SSTA variance.

505 The LIM methodology allows an objective determination of optimal initial condition that
506 evolve into the final specified events (e.g., a mature ENSO event). Using the L2 norm (or

507 Euclidean norm), this amplification factor $\gamma(\tau)$ is quantified as the ratio of the state vector's
 508 magnitude at time τ to its magnitude at the initial time:

509

$$510 \quad \gamma^2(\tau) = \frac{x(\tau)^T x(\tau)}{x(0)^T x(0)} = \frac{x(0)^T G^T(\tau) G(\tau) x(0)}{x(0)^T x(0)}. \quad A9$$

511

512 The optimal initial condition ($x(t) = \phi_1(\tau)$) can then be identified as the first right
 513 eigenvector of $G^T(\tau)G(\tau)$, with $\gamma(\tau)$ the corresponding eigenvalue. The final condition after τ_e
 514 months evolved from ϕ_1 derived by $\tau = \tau_e$ can be expressed as: $x(t + \tau_e) = G(\tau_e)\phi_1(\tau_e)$.

515 For the pacemaker experiment, $\gamma(\tau)$ is the highest at $\tau_e = 6$ to 9 months, which is realized
 516 by the evolution of observed ENSO events of both signs (Penland and Magorian, 1993; Penland
 517 and Sardeshmukh, 1995; Newman et al. 2011a; Newman et al. 2011b; Solomon and Newman
 518 2011). Therefore, to apply LIM analysis for filtering out the evolving ENSO phenomenon, it is
 519 necessary to remove both the optimal initial condition and its resulting evolution.

520 Following Solomon and Newman (2011), we used a LIM to remove ENSO's influence on
 521 SSTAs by constructing a filter specifically removing only variability that actually evolves from
 522 the optimal initial condition through a mature ENSO event. The filter is constructed in the
 523 following steps: (1) the projection on $\phi_1(\tau_e)$ at time $t = t_i$ is determined and its subsequent linear
 524 evolution over the time interval $t = [t_i, t_{i+\tau_1}]$ removed. (2) the projection on $\phi_1(\tau_e)$ of the residual
 525 anomaly at time $t = t_{i+1}$ is determined and the process is repeated. Specifically:

526

$$527 \quad \text{For } t = 0: \alpha(0) = \phi_1(\tau_e) \cdot x(0) \quad A10$$

$$528 \quad R(0) = x(0) - \alpha(0)G(0)\phi_1(\tau_e) \quad A11$$

$$529 \quad \text{For } t = 1: \alpha(1) = \phi_1(\tau_e) \cdot (x(1) - \alpha(0)G(1)\phi_1(\tau_e)) \quad A12$$

$$530 \quad R(1) = x(1) - \alpha(0)G(1)\phi_1(\tau_e) - \alpha(1)G(0)\phi_1(\tau_e) \quad A13$$

531

...

$$532 \quad \text{For } t = n: \alpha(n) = \phi_1(\tau_e) \cdot (x(n) - \sum_{\tau=1}^{\tau_1} \alpha(n - \tau)G(\tau)\phi_1(\tau_e)) \quad A14$$

$$533 \quad R(n) = x(n) - \sum_{\tau=0}^{\tau_1} \alpha(n - \tau)G(\tau)\phi_1(\tau_e) \quad A15$$

534

535 where α is the projection of $\phi_1(\tau_e)$ on the SSTA at that point in the iteration and the summations
 536 are over τ .

537 We remove the evolution of a projection on $\phi_1(\tau_e = 3)$ over $\tau_1 = 25$ months in our filter.
538 The use of $\tau_e = 3$ months follows Solomon and Newman (2011); we also tried $\tau_e = 3$ from 4-8
539 months, but the evolution is quite similar and filtering it yields similar results.

540

541 *5. Evaluation Metrics*

542 To quantify how well each method removes the ENSO signal from SSTAs, we employed two
543 metrics. The first is the correlation between T'_X at each grid point and the Niño3.4 index at several
544 lags (SSTA lagging Niño3.4), where the subscript X represents the different estimates of T'_{EF}
545 generated using the methods described above. Note that it is critical that a method remove the
546 ENSO correlation across a range of lags. For example, removing the 0-month-lag ENSO regression
547 by definition eliminates the simultaneous correlation with Niño3.4, but may fail to remove the
548 ENSO signal at other lags.

549 While a method that completely removes the ENSO signal would have negligible
550 correlation at all lags, a successful method must also remove the ENSO signal while
551 simultaneously leaving the internal variability unrelated to ENSO unaffected. As an extreme but
552 illustrative example, if we were to remove the first 50 EOFs, the resulting SSTAs would have near-
553 zero correlation with Niño3.4 and the method would be excellent as judged by our first metric.
554 However, because those 50 EOFs contain much of the explained variance, the SSTAs themselves
555 would be near zero and thus give little information about variability unrelated to ENSO. Therefore,
556 our second metric compares the variance of T'_X to the variance of T'_{EF} . To a first order, SSTA
557 variance controls the MHW threshold, which is often calculated as the 90th percentile of SSTAs at
558 a given location and time of year (Oliver et al., 2021). Thus, having the correct “ENSO-free”
559 variance is highly important to “ENSO-free” MHW statistics.

560 We must also compensate for the small ensemble size of the CESM2-TPACE. At each time
561 step there will be an error in calculating the “true” or population ensemble mean in Eq. 1 (i.e.,
562 $\langle T' \rangle$) which is normally distributed with a mean of zero and variance $\sigma^2[T']/N_{ens}$, where N_{ens} is the
563 ensemble size (e.g., Leith, 1973). In effect, some of the non-ENSO internal variability is
564 inadvertently incorporated into the ensemble mean because of the finite sample size. Due to the
565 relatively small ensemble size of CESM2-TPACE ($N_{ens}=10$), this error can be non-negligible,
566 particularly in areas of high SST variability.

567 This error also affects our variance comparison metric, since T'_{PM} is inflated by an
 568 additional component of $\sigma^2[T']/N_{ens}$ compared with the case where the true population mean was
 569 used instead of the sample mean (Matsumura et al., 2010; Rowell et al., 1995). To account for this
 570 error, we subtracted the excess variance to compute an estimate of the true ENSO-free variance:

$$571 \sigma_{true}^2[T'_{EF}] \approx \sigma^2[T'_{EF}] - \frac{\sigma^2[T']}{N_{ens}}. \quad A16$$

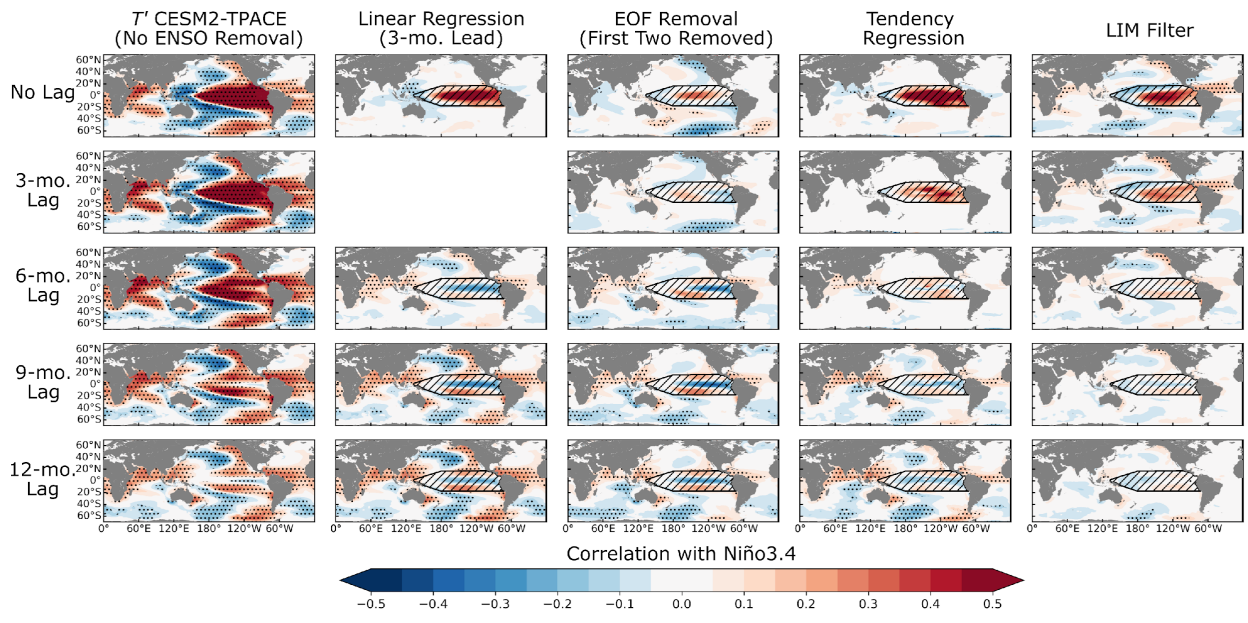
572
 573
 574 To test the significance of the Niño3.4 correlation, we then use the method of Ebisuzaki
 575 (1997). We generated 500 synthetic ENSO indices that have Fourier coefficients of the same
 576 modulus as the original ENSO index, but with randomized phases at each frequency. Thus, the
 577 synthetic ENSO indices have the same spectral and autocorrelation characteristics as the original
 578 index, but are independent. At each grid point, for each ensemble member, we computed the
 579 correlation between T'_{EF} and all 100 synthetic ENSO indices to build up a probability density
 580 function for the absolute value of the correlation. The 95th percentile of this probability density
 581 function is the threshold over which a correlation between the ENSO-removed SSTAs and the real
 582 ENSO index is considered to be statistically significant.

583 To test the significance of the difference in variance, we employ the F -test while
 584 accounting for temporal autocorrelation of the data when estimating the effective degrees of
 585 freedom (Preisendorfer et al., 1981). Because the effective degrees of freedom for the pacemaker
 586 ensemble are on the order of 10^3 - 10^4 , virtually all differences in variance shown in Fig. A2 are
 587 significant at the 95th-percentile level.

588 589 6. Evaluating different ENSO-removal methods

590 Fig. A1 shows the correlation of the ENSO-free SSTAs calculated by each method as a function
 591 of lag (SST lagging Niño3.4). The Linear Regression (with a Niño3.4 lead of three months)
 592 performs well at zero lag, but its efficacy declines as the lag increases (the correlation at three
 593 months lag is zero by construction). At 12 months lag, it is hardly better than if ENSO's influence
 594 had not been removed at all. The EOF Removal method has some areas of significant correlation
 595 at all lags. Note that as more EOFs are removed, the correlation at all lags decreases (see
 596 Supplementary Fig. S7). However, as we will discuss, removing more EOFs begins to remove
 597 variability unrelated to ENSO, limiting the utility of this method. The Tendency Regression

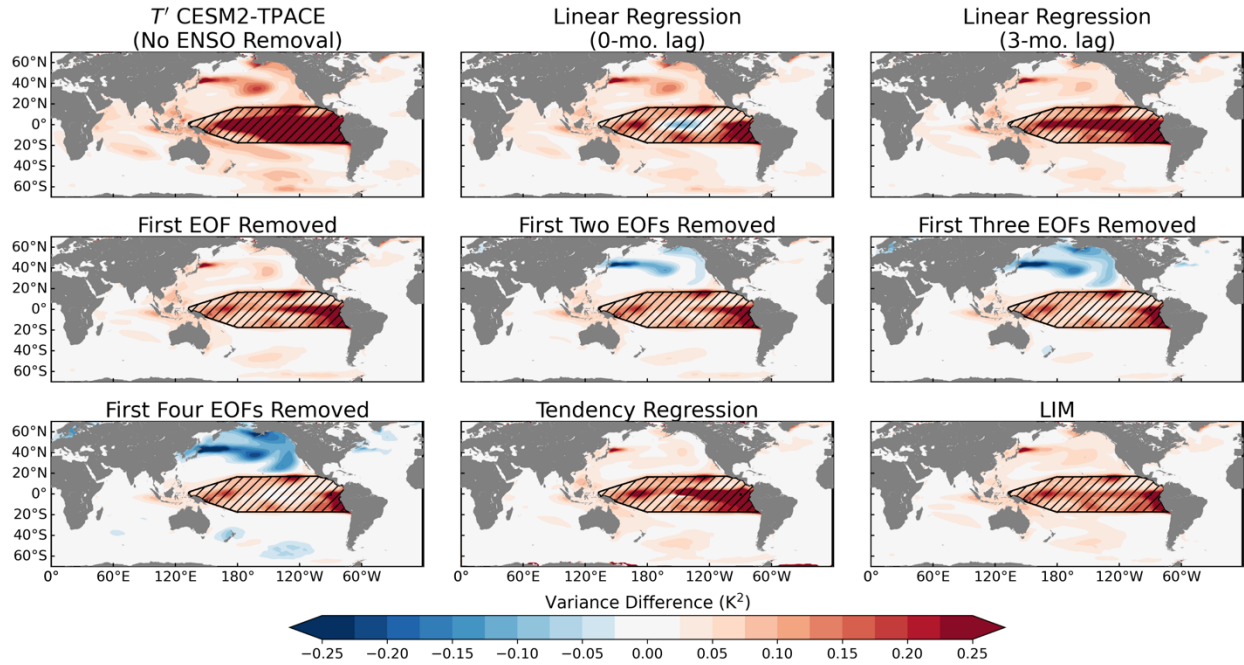
598 performs excellently at zero through six months lag, but its performance declines to a level similar
 599 to the EOF method at lags of nine and 12 months. The LIM Filter method is worse than the
 600 Tendency Regression method at lags zero to six months, but is the best of all methods at nine and
 601 12 months.



602
 603 **Fig. A1.** Correlation between T' (i.e., total SSTAs) and the ensemble mean Niño3.4 in CESM2-
 604 TPACE (first column). Correlation between T'_X (i.e., “ENSO-free” SSTAs) from each of our
 605 ENSO-removal methods and the ensemble mean Niño3.4 in CESM2-TPACE (second through fifth
 606 columns). Each row depicts different lags (SST lagging Niño3.4). The pacemaker nudging region
 607 is outlined and hatched. Areas with correlations significant above the 95th-percentile are stippled.
 608

609 Fig. A2 shows the difference between the ENSO-free SSTA variance calculated using
 610 CESM2-TPACE and the variance of the SSTAs resulting from our methods. The Linear
 611 Regression method retains a considerable amount of variance associated with ENSO, particularly
 612 in the Pacific and Indian Oceans. The EOF Removal method’s performance depends on how many
 613 EOFs are removed. If only the first EOF is removed, the variance is greater than the true ENSO-
 614 free variance, similar to the Linear Regression method. If the first two or more EOFs are removed,
 615 the variance in the North Pacific is progressively underestimated. This is to be expected if the
 616 higher-mode EOFs represent internal variability unrelated to ENSO. The Tendency Regression

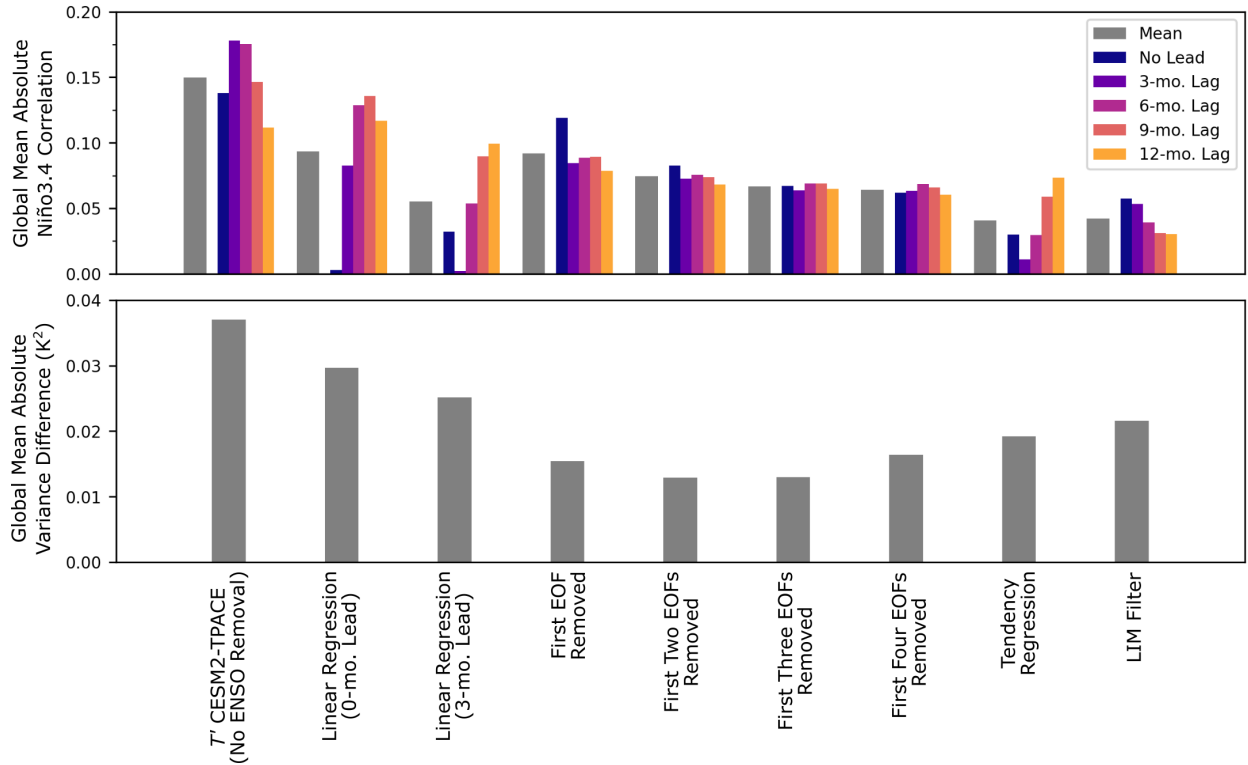
617 and LIM Filter methods have variance greater than the “ENSO-free” variance, although to a much
 618 lesser degree than the Linear Regression method.



619 **Fig. A2.** Difference between the variance of T'_X and T'_{EF} . The top left panel compares the variance
 620 of T' from the CESM2-TPACE to T'_{EF} , representing the case where the ENSO signal is not
 621 removed. Red shading here indicates where ENSO most strongly influences SSTA variance. In all
 622 other panels, areas where too little ENSO variance is removed are shown in red shades; areas
 623 where too much SST variance is removed are shown in blue shades. White indicates that the
 624 method produces a result that matches the ENSO-free SSTA variance. Virtually all differences in
 625 variance are significant at the 95th-percentile level, thus significance is not shown here. The
 626 pacemaker nudging region is outlined and hatched.

627
 628 Except for the EOF Removal method (with two or more EOFs removed), all other methods
 629 overestimate the variance in the central North Pacific, which implies that these methods do not
 630 fully remove the ENSO teleconnection in that basin. The corresponding teleconnection pattern in
 631 the South Pacific is also apparent, although the difference in variance is less than in the North
 632 Pacific. These methods also overestimate the variance in the Kuroshio-Oyashio Extension region.
 633 That some of greatest differences occur in areas of high internal variability (e.g., western boundary
 634 currents) suggests that our compensation for the variance inflation, which is proportional to SST
 635 variance (Eq. A16) was not entirely sufficient to remove the error due to the small ensemble size
 636 and that our methods may indeed perform better than Fig. A2 shows.

637
 638



639

640 **Fig. A3.** Area-weighted absolute value mean (from 60°S-60°N, excluding the pacemaker nudging
 641 region) of the Niño3.4 correlations in Fig. A1 (top) and the variance differences between the
 642 variance resulting from each method and the “ENSO-free” variance in Fig A2 (bottom). The
 643 correlation metric is shown for several lags, with the mean in grey.
 644

645 Fig. A3 condenses the results from Fig. A1 and A2 by taking the area-weighted mean of
 646 the absolute value of the lagged correlation and variance difference over 60°S-60°N and excluding
 647 the pacemaker nudging region. Averaged over all months, the Tendency Regression method is the
 648 best at removing the Niño3.4 correlation, followed closely by the LIM Filter method. For the
 649 variance difference metric, the EOF removal method has the best performance if two or three EOFs
 650 are removed. From Fig. A2, removing two EOFs overestimates the ENSO-free variance; removing
 651 three EOFs underestimates it. The Tendency Regression method is the second-best method at
 652 matching the ENSO-free variance, followed by the LIM Filter method. The Linear Regression
 653 method is better than the EOF method at removing the Niño3.4 correlation, but the worst at
 654 reproducing the correct ENSO-free variance.

655 On the basis of these two metrics, we consider the Tendency Regression method to be the
 656 best overall. The LIM Filter method has only slightly worse performance. The primary difference

657 between these two methods is that the Tendency Regression removes the Niño3.4 correlation better
658 at smaller lags, and the LIM Filter method removes that correlation better at longer lags.

659 The Tendency Regression method also has a few practical advantages. It is simple to
660 implement, requiring little judgement beyond selecting an appropriate ENSO index. In contrast,
661 the EOF method requires some subjective judgement when selecting how many EOFs to remove.
662 As more EOFs are removed, the Niño3.4 correlation decreases, but more internal variability
663 unrelated to ENSO is inadvertently removed. Our results suggest that the first two EOFs was the
664 best compromise between these conflicting trends, however, different climate models may have
665 different ENSO behavior and teleconnection (e.g., Maher et al., 2023) and thus different global
666 EOFs, making it difficult to know whether two EOFs are sufficient in other contexts. The LIM
667 Filter method is somewhat more complex than the Tendency Regression method and requires the
668 selection of multiple parameters.

669 The Tendency Regression method also may be easily modified to include other forcing
670 terms into Eq. A3 to investigate the influence of additional climate modes and physical processes
671 on SST variability and MHWs. Because it is fit at each grid point individually, the Tendency
672 Regression method can work with just two time series: an SSTA time series at a given location
673 and an ENSO index. This may be important for applications where the data is sparse (e.g., SST
674 data before about 1960 or paleoclimate proxy data).

675

676

677 **References**

678 Alexander, M. A., Bladé, I., Newman, M., Lanzante, J. R., Lau, N.-C., & Scott, J. D. (2002). The

679 Atmospheric Bridge: The Influence of ENSO Teleconnections on Air–Sea Interaction
680 over the Global Oceans. *Journal of Climate*, 15(16), 2205–2231.

681 [https://doi.org/10.1175/1520-0442\(2002\)015<2205:TABTIO>2.0.CO;2](https://doi.org/10.1175/1520-0442(2002)015<2205:TABTIO>2.0.CO;2)

682 Alexander, M. A., & Deser, C. (1995). A Mechanism for the Recurrence of Wintertime

683 Midlatitude SST Anomalies. *Journal of Physical Oceanography*, 25(1), 122–137.

684 [https://doi.org/10.1175/1520-0485\(1995\)025%3C0122:AMFTRO%3E2.0.CO;2](https://doi.org/10.1175/1520-0485(1995)025%3C0122:AMFTRO%3E2.0.CO;2)

685 Alexander, M., & Scott, J. (2002). The influence of ENSO on air-sea interaction in the Atlantic.
686 *Geophysical Research Letters*, 29(14), 46-1-46-4.
687 <https://doi.org/10.1029/2001GL014347>

688 Amaya, D. J., Jacox, M. G., Fewings, M. R., Saba, V. S., Stuecker, M. F., Rykaczewski, R. R.,
689 Ross, A. C., Stock, C. A., Capotondi, A., Petrik, C. M., Bograd, S. J., Alexander, M. A.,
690 Cheng, W., Hermann, A. J., Kearney, K. A., & Powell, B. S. (2023). Marine heatwaves
691 need clear definitions so coastal communities can adapt. *Nature*, 616(7955), 29–32.
692 <https://doi.org/10.1038/d41586-023-00924-2>

693 Barnston, A. G., Chelliah, M., & Goldenberg, S. B. (1997). Documentation of a highly ENSO-
694 related SST region in the equatorial Pacific. *Atmosphere-Ocean*, 35(3), 367–383.
695 <https://doi.org/10.1080/07055900.1997.9649597>

696 Capotondi, A., Deser, C., Phillips, A. S., Okumura, Y., & Larson, S. M. (2020). ENSO and
697 Pacific Decadal Variability in the Community Earth System Model Version 2. *Journal of*
698 *Advances in Modeling Earth Systems*, 12(12), e2019MS002022.
699 <https://doi.org/10.1029/2019MS002022>

700 Chiang, J. C. H., & Vimont, D. J. (2004). Analogous Pacific and Atlantic Meridional Modes of
701 Tropical Atmosphere–Ocean Variability. *Journal of Climate*, 17(21), 4143–4158.
702 <https://doi.org/10.1175/JCLI4953.1>

703 Compo, G. P., & Sardeshmukh, P. D. (2010). Removing ENSO-Related Variations from the
704 Climate Record. *Journal of Climate*, 23(8), 1957–1978.
705 <https://doi.org/10.1175/2009JCLI2735.1>

706 Danabasoglu, G., Lamarque, J. -F., Bacmeister, J., Bailey, D. A., DuVivier, A. K., Edwards, J.,
707 Emmons, L. K., Fasullo, J., Garcia, R., Gettelman, A., Hannay, C., Holland, M. M.,

708 Large, W. G., Lauritzen, P. H., Lawrence, D. M., Lenaerts, J. T. M., Lindsay, K.,
709 Lipscomb, W. H., Mills, M. J., ... Strand, W. G. (2020). The Community Earth System
710 Model Version 2 (CESM2). *Journal of Advances in Modeling Earth Systems*, 12(2),
711 e2019MS001916. <https://doi.org/10.1029/2019MS001916>

712 De Elvira, A. R., & Lemke, P. (1982). A Langevin equation for stochastic climate models with
713 periodic feedback and forcing variance. *Tellus*, 34(4), 313–320.
714 <https://doi.org/10.1111/j.2153-3490.1982.tb01821.x>

715 Deser, C., Phillips, A. S., Alexander, M. A., Amaya, D. J., Capotondi, A., Jacox, M. G., & Scott,
716 J. D. (2024). Future Changes in the Intensity and Duration of Marine Heat and Cold
717 Waves: Insights from Coupled Model Initial-Condition Large Ensembles. *Journal of*
718 *Climate*, 37(6), 1877–1902. <https://doi.org/10.1175/JCLI-D-23-0278.1>

719 Deser, C., Simpson, I. R., McKinnon, K. A., & Phillips, A. S. (2017). The Northern Hemisphere
720 Extratropical Atmospheric Circulation Response to ENSO: How Well Do We Know It
721 and How Do We Evaluate Models Accordingly? *Journal of Climate*, 30(13), 5059–5082.
722 <https://doi.org/10.1175/JCLI-D-16-0844.1>

723 Ebisuzaki, W. (1997). A Method to Estimate the Statistical Significance of a Correlation When
724 the Data Are Serially Correlated. *Journal of Climate*, 10(9), 2147–2153.
725 [https://doi.org/10.1175/1520-0442\(1997\)010<2147:AMTETS>2.0.CO;2](https://doi.org/10.1175/1520-0442(1997)010<2147:AMTETS>2.0.CO;2)

726 Frankignoul, C. (1985). Sea surface temperature anomalies, planetary waves, and air-sea
727 feedback in the middle latitudes. *Reviews of Geophysics*, 23(4), 357.
728 <https://doi.org/10.1029/RG023i004p00357>

729 Gunnarson, J. L., Stuecker, M. F., & Zhao, S. (2024). Drivers of future extratropical sea surface
730 temperature variability changes in the North Pacific. *Npj Climate and Atmospheric*
731 *Science*, 7(1), 164. <https://doi.org/10.1038/s41612-024-00702-5>

732 Hasselmann, K. (1976). Stochastic climate models. Part I: Theory. *Tellus*, 28(6), 473–485.
733 <https://doi.org/10.1111/j.2153-3490.1976.tb00696.x>

734 Hersbach, H., Bell, B., Berrisford, P., Hirahara, S., Horányi, A., Muñoz-Sabater, J., Nicolas, J.,
735 Peubey, C., Radu, R., Schepers, D., Simmons, A., Soci, C., Abdalla, S., Abellan, X.,
736 Balsamo, G., Bechtold, P., Biavati, G., Bidlot, J., Bonavita, M., ... Thépaut, J.-N. (2020).
737 The ERA5 global reanalysis. *Quarterly Journal of the Royal Meteorological Society*,
738 146(730), 1999–2049. <https://doi.org/10.1002/qj.3803>

739 Huang, B. (2004). Remotely forced variability in the tropical Atlantic Ocean. *Climate Dynamics*,
740 23(2), 133–152. <https://doi.org/10.1007/s00382-004-0443-8>

741 Huang, B., Thorne, P. W., Banzon, V. F., Boyer, T., Chepurin, G., Lawrimore, J. H., Menne, M.
742 J., Smith, T. M., Vose, R. S., & Zhang, H.-M. (2017). Extended Reconstructed Sea
743 Surface Temperature, Version 5 (ERSSTv5): Upgrades, Validations, and
744 Intercomparisons. *Journal of Climate*, 30(20), 8179–8205. [https://doi.org/10.1175/JCLI-](https://doi.org/10.1175/JCLI-D-16-0836.1)
745 [D-16-0836.1](https://doi.org/10.1175/JCLI-D-16-0836.1)

746 Huang, B., Yin, X., Carton, J. A., Chen, L., Graham, G., Hogan, P., Smith, T., & Zhang, H.-M.
747 (2024). Record High Sea Surface Temperatures in 2023. *Geophysical Research Letters*,
748 51(14), e2024GL108369. <https://doi.org/10.1029/2024GL108369>

749 Jiang, N., Zhu, C., Hu, Z.-Z., McPhaden, M. J., Chen, D., Liu, B., Ma, S., Yan, Y., Zhou, T.,
750 Qian, W., Luo, J., Yang, X., Liu, F., & Zhu, Y. (2024). Enhanced risk of record-breaking

751 regional temperatures during the 2023–24 El Niño. *Scientific Reports*, 14(1), 2521.
752 <https://doi.org/10.1038/s41598-024-52846-2>

753 Jiang, N., Zhu, C., Hu, Z.-Z., McPhaden, M. J., Lian, T., Zhou, C., Qian, W., & Chen, D. (2025).
754 El Niño and Sea Surface Temperature Pattern Effects Lead to Historically High Global
755 Mean Surface Temperatures in 2023. *Geophysical Research Letters*, 52(2),
756 e2024GL113733. <https://doi.org/10.1029/2024GL113733>

757 Johnson, G. C., Lumpkin, R., Alexander, M. A., Amaya, D. J., Beckley, B., Boyer, T., Bringas,
758 F., Carter, B. R., Cetinić, I., Chambers, D. P., Chan, D., Cheng, L., Dong, S., Elipot, S.,
759 Feely, R. A., Franz, B. A., Fu, Y., Gao, M., Garg, J., ... Zhang, H. (2024). Global
760 Oceans. *Bulletin of the American Meteorological Society*, 105(8), S156–S213.
761 <https://doi.org/10.1175/BAMS-D-24-0100.1>

762 Kelly, P. M., & Jones, P. D. (1996). Removal of the El Niño-Southern Oscillation signal from
763 the gridded surface air temperature data set. *Journal of Geophysical Research:*
764 *Atmospheres*, 101(D14), 19013–19022. <https://doi.org/10.1029/96JD01173>

765 Klein, S. A., Soden, B. J., & Lau, N.-C. (1999). Remote Sea Surface Temperature Variations
766 during ENSO: Evidence for a Tropical Atmospheric Bridge. *Journal of Climate*, 12(4),
767 917–932. [https://doi.org/10.1175/1520-0442\(1999\)012<0917:RSSTVD>2.0.CO;2](https://doi.org/10.1175/1520-0442(1999)012<0917:RSSTVD>2.0.CO;2)

768 Larson, S. M., Vimont, D. J., Clement, A. C., & Kirtman, B. P. (2018). How Momentum
769 Coupling Affects SST Variance and Large-Scale Pacific Climate Variability in CESM.
770 *Journal of Climate*, 31(7), 2927–2944. <https://doi.org/10.1175/JCLI-D-17-0645.1>

771 Lau, N.-C., & Nath, M. J. (1994). A Modeling Study of the Relative Roles of Tropical and
772 Extratropical SST Anomalies in the Variability of the Global Atmosphere-Ocean System.

773 *Journal of Climate*, 7(8), 1184–1207. <https://doi.org/10.1175/1520->
774 0442(1994)007<1184:AMSOTR>2.0.CO;2

775 Lau, N.-C., & Nath, M. J. (1996). The Role of the “Atmospheric Bridge” in Linking Tropical
776 Pacific ENSO Events to Extratropical SST Anomalies. *Journal of Climate*, 9(9), 2037–
777 2057. [https://doi.org/10.1175/1520-0442\(1996\)009<2036:TROTBI>2.0.CO;2](https://doi.org/10.1175/1520-0442(1996)009<2036:TROTBI>2.0.CO;2)

778 Leith, C. E. (1973). The Standard Error of Time-Average Estimates of Climatic Means. *Journal*
779 *of Applied Meteorology and Climatology*, 12(6), 1066–1069.
780 [https://doi.org/10.1175/1520-0450\(1973\)012<1066:TSEOTA>2.0.CO;2](https://doi.org/10.1175/1520-0450(1973)012<1066:TSEOTA>2.0.CO;2)

781 Maher, N., Wills, R. C. J., DiNezio, P., Klavans, J., Milinski, S., Sanchez, S. C., Stevenson, S.,
782 Stuecker, M. F., & Wu, X. (2023). The future of the El Niño–Southern Oscillation: Using
783 large ensembles to illuminate time-varying responses and inter-model differences. *Earth*
784 *System Dynamics*, 14(2), 413–431. <https://doi.org/10.5194/esd-14-413-2023>

785 Matsumura, S., Huang, G., Xie, S.-P., & Yamazaki, K. (2010). SST-Forced and Internal
786 Variability of the Atmosphere in an Ensemble GCM Simulation. *Journal of the*
787 *Meteorological Society of Japan. Ser. II*, 88(1), 43–62. <https://doi.org/10.2151/jmsj.2010->
788 104

789 Mo, K. C. (2000). Relationships between Low-Frequency Variability in the Southern
790 Hemisphere and Sea Surface Temperature Anomalies. *Journal of Climate*, 13(20), 3599–
791 3610. [https://doi.org/10.1175/1520-0442\(2000\)013<3599:RBLFVI>2.0.CO;2](https://doi.org/10.1175/1520-0442(2000)013<3599:RBLFVI>2.0.CO;2)

792 Mo, K. C., & Higgins, R. W. (1998). The Pacific–South American Modes and Tropical
793 Convection during the Southern Hemisphere Winter. *Monthly Weather Review*, 126(6),
794 1581–1596. [https://doi.org/10.1175/1520-0493\(1998\)126<1581:TPSAMA>2.0.CO;2](https://doi.org/10.1175/1520-0493(1998)126<1581:TPSAMA>2.0.CO;2)

795 Newman, M., Alexander, M. A., Ault, T. R., Cobb, K. M., Deser, C., Di Lorenzo, E., Mantua, N.
796 J., Miller, A. J., Minobe, S., Nakamura, H., Schneider, N., Vimont, D. J., Phillips, A. S.,
797 Scott, J. D., & Smith, C. A. (2016). The Pacific Decadal Oscillation, Revisited. *Journal*
798 *of Climate*, 29(12), 4399–4427. <https://doi.org/10.1175/JCLI-D-15-0508.1>

799 Newman, M., Compo, G. P., & Alexander, M. A. (2003). ENSO-Forced Variability of the
800 Pacific Decadal Oscillation. *Journal of Climate*, 16(23), 3853–3857.
801 [https://doi.org/10.1175/1520-0442\(2003\)016<3853:EVOTPD>2.0.CO;2](https://doi.org/10.1175/1520-0442(2003)016<3853:EVOTPD>2.0.CO;2)

802 Nicholls, N. (1984). The Southern Oscillation and Indonesian Sea Surface Temperature. *Monthly*
803 *Weather Review*, 112(3), 424–432. [https://doi.org/10.1175/1520-0493\(1984\)112<0424:TSOAIS>2.0.CO;2](https://doi.org/10.1175/1520-0493(1984)112<0424:TSOAIS>2.0.CO;2)

805 Oliver, E. C. J., Benthuisen, J. A., Darmaraki, S., Donat, M. G., Hobday, A. J., Holbrook, N. J.,
806 Schlegel, R. W., & Sen Gupta, A. (2021). Marine Heatwaves. *Annual Review of Marine*
807 *Science*, 13(1), 313–342. <https://doi.org/10.1146/annurev-marine-032720-095144>

808 Oliver, E. C. J., Donat, M. G., Burrows, M. T., Moore, P. J., Smale, D. A., Alexander, L. V.,
809 Benthuisen, J. A., Feng, M., Sen Gupta, A., Hobday, A. J., Holbrook, N. J., Perkins-
810 Kirkpatrick, S. E., Scannell, H. A., Straub, S. C., & Wernberg, T. (2018). Longer and
811 more frequent marine heatwaves over the past century. *Nature Communications*, 9(1),
812 1324. <https://doi.org/10.1038/s41467-018-03732-9>

813 Park, S., Alexander, M. A., & Deser, C. (2006). The Impact of Cloud Radiative Feedback,
814 Remote ENSO Forcing, and Entrainment on the Persistence of North Pacific Sea Surface
815 Temperature Anomalies. *Journal of Climate*, 19(23), 6243–6261.
816 <https://doi.org/10.1175/JCLI3957.1>

817 Penland, C., & Matrosova, L. (2006). Studies of El Niño and Interdecadal Variability in Tropical
818 Sea Surface Temperatures Using a Nonnormal Filter. *Journal of Climate*, 19(22), 5796–
819 5815. <https://doi.org/10.1175/JCLI3951.1>

820 Penland, C., & Sardeshmukh, P. D. (1995). The Optimal Growth of Tropical Sea Surface
821 Temperature Anomalies. *Journal of Climate*, 8(8), 1999–2024.
822 [https://doi.org/10.1175/1520-0442\(1995\)008%3C1999:TOGOTS%3E2.0.CO;2](https://doi.org/10.1175/1520-0442(1995)008%3C1999:TOGOTS%3E2.0.CO;2)

823 Preisendorfer, R. W., Zwiers, F. W., & Barnett, T. P. (1981). *Foundations of Principle*
824 *Component Selection Rules*. Scripps Institution of Oceanography.

825 Rayner, N. A., Parker, D. E., Horton, E. B., Folland, C. K., Alexander, L. V., Rowell, D. P.,
826 Kent, E. C., & Kaplan, A. (2003). Global analyses of sea surface temperature, sea ice,
827 and night marine air temperature since the late nineteenth century. *Journal of*
828 *Geophysical Research: Atmospheres*, 108(D14). <https://doi.org/10.1029/2002JD002670>

829 Robock, A., & Mao, J. (1995). The Volcanic Signal in Surface Temperature Observations.
830 *Journal of Climate*, 8(5), 1086–1103. [https://doi.org/10.1175/1520-](https://doi.org/10.1175/1520-0442(1995)008<1086:TVSIST>2.0.CO;2)
831 [0442\(1995\)008<1086:TVSIST>2.0.CO;2](https://doi.org/10.1175/1520-0442(1995)008<1086:TVSIST>2.0.CO;2)

832 Rodgers, K. B., Lee, S.-S., Rosenbloom, N., Timmermann, A., Danabasoglu, G., Deser, C.,
833 Edwards, J., Kim, J.-E., Simpson, I. R., Stein, K., Stuecker, M. F., Yamaguchi, R., Bódai,
834 T., Chung, E.-S., Huang, L., Kim, W. M., Lamarque, J.-F., Lombardozzi, D. L., Wieder,
835 W. R., & Yeager, S. G. (2021). Ubiquity of human-induced changes in climate
836 variability. *Earth System Dynamics*, 12(4), 1393–1411. [https://doi.org/10.5194/esd-12-](https://doi.org/10.5194/esd-12-1393-2021)
837 [1393-2021](https://doi.org/10.5194/esd-12-1393-2021)

838 Rodrigues, R. R., Campos, E. J. D., & Haarsma, R. (2015). The Impact of ENSO on the South
839 Atlantic Subtropical Dipole Mode. *Journal of Climate*, 28(7), 2691–2705.
840 <https://doi.org/10.1175/JCLI-D-14-00483.1>

841 Rodrigues, R. R., Haarsma, R. J., Campos, E. J. D., & Ambrizzi, T. (2011). The Impacts of
842 Inter–El Niño Variability on the Tropical Atlantic and Northeast Brazil Climate. *Journal*
843 *of Climate*, 24(13), 3402–3422. <https://doi.org/10.1175/2011JCLI3983.1>

844 Rowell, D. P., Folland, C. K., Maskell, K., & Ward, M. N. (1995). Variability of summer rainfall
845 over tropical north Africa (1906–92): Observations and modelling. *Quarterly Journal of*
846 *the Royal Meteorological Society*, 121(523), 669–704.
847 <https://doi.org/10.1002/qj.49712152311>

848 Saji, N. H., Goswami, B. N., Vinayachandran, P. N., & Yamagata, T. (1999). A dipole mode in
849 the tropical Indian Ocean. *Nature*, 401(6751), 360–363. <https://doi.org/10.1038/43854>

850 Santer, B. D., Wigley, T. M. L., Doutriaux, C., Boyle, J. S., Hansen, J. E., Jones, P. D., Meehl,
851 G. A., Roeckner, E., Sengupta, S., & Taylor, K. E. (2001). Accounting for the effects of
852 volcanoes and ENSO in comparisons of modeled and observed temperature trends.
853 *Journal of Geophysical Research: Atmospheres*, 106(D22), 28033–28059.
854 <https://doi.org/10.1029/2000JD000189>

855 Schneider, N., & Cornuelle, B. D. (2005). The Forcing of the Pacific Decadal Oscillation.
856 *Journal of Climate*, 18(21), 4355–4373. <https://doi.org/10.1175/JCLI3527.1>

857 Smith, K. E., Sen Gupta, A., Amaya, D., Benthuisen, J. A., Burrows, M. T., Capotondi, A.,
858 Filbee-Dexter, K., Frölicher, T. L., Hobday, A. J., Holbrook, N. J., Malan, N., Moore, P.
859 J., Oliver, E. C. J., Richaud, B., Salcedo-Castro, J., Smale, D. A., Thomsen, M., &
860 Wernberg, T. (2025). Baseline matters: Challenges and implications of different marine

861 heatwave baselines. *Progress in Oceanography*, 231, 103404.
862 <https://doi.org/10.1016/j.pocean.2024.103404>

863 Solomon, A., & Newman, M. (2012). Reconciling disparate twentieth-century Indo-Pacific
864 ocean temperature trends in the instrumental record. *Nature Climate Change*, 2(9), 691–
865 699. <https://doi.org/10.1038/nclimate1591>

866 Sprintall, J., Cravatte, S., Dewitte, B., Du, Y., & Gupta, A. S. (2020). ENSO Oceanic
867 Teleconnections. In *El Niño southern oscillation in a changing climate* (pp. 337–360).
868 Wiley.

869 Stuecker, M. F., Timmermann, A., Jin, F., Chikamoto, Y., Zhang, W., Wittenberg, A. T.,
870 Widiasih, E., & Zhao, S. (2017). Revisiting ENSO/Indian Ocean Dipole phase
871 relationships. *Geophysical Research Letters*, 44(5), 2481–2492.
872 <https://doi.org/10.1002/2016GL072308>

873 Stuecker, M. F., Timmermann, A., Jin, F.-F., McGregor, S., & Ren, H.-L. (2013). A combination
874 mode of the annual cycle and the El Niño/Southern Oscillation. *Nature Geoscience*, 6(7),
875 540–544. <https://doi.org/10.1038/ngeo1826>

876 Taschetto, A. S., Ummenhofer, C. C., Stuecker, M. F., Dommenges, D., Ashok, K., Rodrigues,
877 R. R., & Sang-Wook, Y. (2020). ENSO Atmospheric Teleconnections. In *El Niño*
878 *southern oscillation in a changing climate* (First Edition, pp. 311–335). Wiley-American
879 Geophysical Union.

880 Timmermann, A., An, S.-I., Kug, J.-S., Jin, F.-F., Cai, W., Capotondi, A., Cobb, K. M.,
881 Lengaigne, M., McPhaden, M. J., Stuecker, M. F., Stein, K., Wittenberg, A. T., Yun, K.-
882 S., Bayr, T., Chen, H.-C., Chikamoto, Y., Dewitte, B., Dommenges, D., Grothe, P., ...

883 Zhang, X. (2018). El Niño–Southern Oscillation complexity. *Nature*, *559*(7715), 535–
884 545. <https://doi.org/10.1038/s41586-018-0252-6>

885 Xu, T., Newman, M., Capotondi, A., Stevenson, S., Di Lorenzo, E., & Alexander, M. A. (2022).
886 An increase in marine heatwaves without significant changes in surface ocean
887 temperature variability. *Nature Communications*, *13*(1), 7396.
888 <https://doi.org/10.1038/s41467-022-34934-x>

889 Zhao, S., Jin, F., & Stuecker, M. F. (2019). Improved Predictability of the Indian Ocean Dipole
890 Using Seasonally Modulated ENSO Forcing Forecasts. *Geophysical Research Letters*,
891 *46*(16), 9980–9990. <https://doi.org/10.1029/2019GL084196>

892 Zhao, Y., Newman, M., Capotondi, A., Lorenzo, E. D., & Sun, D. (2021). Removing the Effects
893 of Tropical Dynamics from North Pacific Climate Variability. *Journal of Climate*,
894 *34*(23), 9249–9265. <https://doi.org/10.1175/JCLI-D-21-0344.1>

895